Check for updates

The anti-correlation effect of alkyl chain size on the photovoltaic performance of centrally extended non-fullerene acceptors†

Tainan Duan, [ID] ‡[ad] Jia Wang,‡[a] Xiaochan Zuo,‡[c] Xingqi Bi,‡[b] Cheng Zhong,*[e] Yulu Li,[d] Yuhong Long,[b] Kaihuai Tu,[d] Weichao Zhang,[f] Ke Yang,[d] Huiqiong Zhou, [ID] [f] Xiangjian Wan, [ID] [b] Yan Zhao,*[c] Bin Kan*[a] and Yongsheng Chen [ID] *[b]

Contrary to previous results, a unique anti-correlation effect of the alkyl chain size on the photovoltaic performance of acceptors was observed. For a centrally-extended acceptor, replacing linear alkyl chains (*n*-undecyl for CH-BBQ) on the thienothiophene unit with branched ones (2-butyloctyl for CH-BO) leads to a plunge in the power conversion efficiency of organic solar cells (18.12% *vs.* 11.34% for binary devices), while the largely shortened ones (*n*-heptyl for CH-HP) bring a surge in performance (18.74%/19.44% for binary/ternary devices). Compared with CH-BO, the more compact intermolecular packing of CH-HP facilitates carrier transport. The characterization of organic field effect transistors and carrier dynamics also echoes the above results. Molecular dynamics simulations indicate that the encounter of the branched alkyl chains and the extended central core hinders the effective interfacial interaction of polymer donors and acceptors, thus deteriorating the device performance. This work suggests that the conventional strategy for alkyl chain engineering of Y-series acceptors might need to be reconsidered in other molecular systems.

New concepts

The side chain branching strategy has achieved a triumph in the modification of the Y-series non-fullerene acceptor (NFA) and pushed the efficiencies of organic photovoltaics to over 19%. However, its applicability to other NFA systems might need reconsideration. For a benzobisthiadiazole-embedded centrally extended π-backbone, the introduction of 2-butyloctyl side chains has yielded suboptimal power conversion efficiency (PCE of 11.3%). Conversely, the adoption of miniaturized *n*-heptyl side chains has precipitated a notable upsurge in photovoltaic performance (PCE of 19.44%). Subsequent analysis has unveiled that the superior performance associated with the latter configuration can be attributed to a more compact molecular packing of the NFA, coupled with a more favorable intermolecular arrangement with PM6, engendered by the synergistic effects of shortened side chains and an extended central core. Our study furnishes novel insights into the interaction between the two primary stacking motifs observed in NFAs, thereby elucidating reference principles for optimizing alkyl chains in centrally extended NFAs. Additionally, our findings propose new guidelines, advocating for the incorporation of an extended core alongside shortened alkyl chains, as a strategic approach for molecular engineering aimed at achieving high-performance NFAs.

Introduction

Organic solar cells (OSCs) are garnering continuous attention due to their solution-processability and capability of constructing flexible devices.[1,2] In the architecture of OSCs, the component of electron donor–acceptor (D–A) bulk-heterojunction (BHJ) blends plays a decisive role in determining the power conversion efficiency (PCE) of the devices.[3,4] In recent years, the development of "Acceptor–Donor–Acceptor" ("A–D–A") structured non-fullerene

[a] School of Materials Science and Engineering, National Institute for Advanced Materials, Nankai University, Tianjin, 300350, China. E-mail: kanbin04@nankai.edu.cn

[b] State Key Laboratory and Institute of Elemento-Organic Chemistry, The Centre of Nanoscale Science and Technology and Key Laboratory of Functional Polymer Materials, Renewable Energy Conversion and Storage Center (RECAST), College of Chemistry, Nankai University, Tianjin, 300071, China. E-mail: yschen99@nankai.edu.cn

[c] Laboratory of Molecular Materials and Devices, Department of Materials Science, Fudan University, Shanghai 200438, China. E-mail: zhaoy@fudan.edu.cn

[d] Chongqing Institute of Green and Intelligent Technology, Chongqing School, University of Chinese Academy of Sciences (UCAS Chongqing), Chinese Academy of Sciences, Chongqing, 400714, China

[e] Hubei Key Laboratory on Organic and Polymeric Opto-electronic Materials, College of Chemistry and Molecular Sciences, Wuhan University, Wuhan, 430072, China. E-mail: zhongcheng@whu.edu.cn

[f] CAS Key Laboratory of Nanosystem and Hierarchical Fabrication, National Center for Nanoscience and Technology, Beijing 100190, P. R. China

† Electronic supplementary information (ESI) available. CCDC 2300122 and 2321689. For ESI and crystallographic data in CIF or other electronic format see DOI: https://doi.org/10.1039/d4mh00699b

‡ These authors contributed equally to this work.

acceptors (NFAs), especially the revolutionary ITIC-[5] and Y-series NFAs,[6] not only brought the surge in the PCE of OSC devices,[7–11] but also renewed the understanding of the relationship between the molecular structure of the acceptor and the corresponding device performance.[12]

With the observation of high-performance A–D–A structured NFAs, the fine-tuning of the intermolecular packing and the morphology of donor–acceptor (D–A) blends are essential for OSC device optimization.[13,14] Therefore, understanding the pattern of the intermolecular stacking of NFAs is not only mandatory for elucidating their working mechanism, but also indispensable for further molecular modification.[15–17] At first, ITIC-series NFAs revealed that face-to-face packing between terminal groups of adjacent molecules might facilitate efficient charge transfer.[18] Later, Y-series NFAs demonstrated a central core involving a three-dimensional (3D) interpenetrating network, indicating that the central core not only regulates the energy levels of the acceptor, but also influences its stacking pattern.[19] Moreover, some significant differences in stacking mode between the ITIC- and Y-series NFAs have been observed due to the variation of alkyl chains. Compared with the ITIC-series that contain spatially orthogonal alkyl chains on the sp^3 hybrid carbon, the N-alkyl chains in Y-series NFAs lead to reduced steric hindrance, and consequently, a more compact framework with multiple interconnected charge transport channels can thus be generated.[20] Hence, the synergistic interaction among the central core, end-groups, and alkyl chains determines the stacking patterns and even all properties of an NFA.

As one of three main stacking motifs in constructing a typical Y-series NFA molecule, the solubilizing flexible alkyl chains can sometimes exert a greater impact on the device performance than the rigid terminal groups and central core do due to their higher variability and diversity.[21,22] Hundreds of attempts have been made in the hope of improving the PCE, but only a few were proven to be effective.[23–26] As one of the most effective attempts in alkyl chain engineering, L8-BO, synthesized via substituting the beta position of the thiophene unit on the Y6 molecule with a branched 2-butyloctyl (BO) chain, shows a solid improvement in performance.[27] Compared with Y6, the introduction of a branched alkyl chain gives the upshifted lowest unoccupied molecular orbital (LUMO) energy level and improved open-circuit voltage (V_{OC}); more importantly, the BO group endows L8-BO with distinct self-packing and intermolecular interaction modes with polymer donors. From Y6 to L8-BO, not only the single-crystal space group was changed from triclinic to monoclinic, but the packing coefficient also enhanced from 54.5% to 64.1%, leading to densified molecular assembly, a long-range order with a higher degree of crystallinity, and increased charge-hopping channels in L8-BO.[22,28] Moreover, after blending with polymer donors, an unprecedented refined double-fibril network can be generated along with the optimized D–A interfacial interaction in L8-BO based blends.[9,29] Consequently, synergistically modified charge generation/transport and an enhanced PCE of over 19% can be obtained. The "alkyl chain branching" strategy provides an essential improvement in the photovoltaic performance of Y-series NFAs, and several following research studies validated the superiority of L8-BO and the effectiveness of such a strategy. However, when the central core of Y-series NFAs also started to engage in extension, the situation became more delicate and complicated.

Recently, a new molecular design strategy of "central core extension" was developed, and the corresponding CH-series NFAs could result in a multimodal and compact intermolecular packing in a single crystal.[30–35] Therefore, charge transport could be improved due to reduced energetic disorder in blend films, together with reduced nonradiative recombination loss.[36,37] Thus, enhanced PCE with high V_{OC} can be simultaneously achieved.[38] Although different stacking motifs are involved, the two above-mentioned strategies share one thing in common: they can both enhance the performance of NFA by prompting the formation of a more condensed intermolecular packing network with more interconnected charge transport/hopping channels in NFA molecules.[39] However, it can be inferred that as the central core extends and the contribution of the central core to the intermolecular packing increases, the impact of alkyl chains on the packing mode of NFAs along with their influence on the pattern of D–A interfacial interactions might differ significantly from that in Y-series NFAs. Hereon, questions naturally arise: could branched alkyl chains still work well with the centrally extended NFAs? If not, how can centrally extended NFAs find a suitable alkyl chain to pair with?

In this contribution, a unique anti-correlation effect of the alkyl chain size on the photovoltaic performance of centrally extended NFAs was discovered and investigated. Recently, the effect of electron-deficient conjugation extended central cores on the photovoltaic performance of NFAs was investigated, and benzobisthiadiazole-embedded NFA CH-BBQ was approved to have a promising PCE of over 18.1%. Taking CH-BBQ as a reference, two analogues with branched (2-butyloctyl for CH-BO) and shortened linear (n-heptyl for CH-HP) alkyl chains were constructed to explore how the alkyl chain size impacts the photovoltaic performance of centrally extended NFAs (Fig. 1a). Different from previous reports, alkyl chain branching is counter-productive in this case. CH-BO not only exhibits drastically blue-shifted absorption, but also displays loosened intermolecular stacking with a lower packing density revealed by single crystal X-ray diffraction; in contrast, CH-HP with shortened alkyl chains exhibits a red-shifted absorption and more ordered intermolecular stacking with a higher packing density. Moreover, CH-BO and CH-HP exhibited polarized charge transport behaviors. By employed in the devices of single crystal organic field effect transistors (OFETs), CH-BO exhibited inferior electron transporting capability with an electron mobility (μ_e) of 0.01 cm^2 V^{-1} s^{-1} while CH-HP exhibited a nearly 16-fold value of 0.16 cm^2 V^{-1} s^{-1}. After being adopted in OSC devices using PM6 as a polymer donor, the CH-BO based binary system showed a low PCE of 11.43% with an inferior short-circuit current density (J_{SC}) of 17.46 mA cm^{-2} and a fill factor (FF) of 66.9%, respectively; in contrast, PM6:CH-HP based devices demonstrated a high PCE of 18.74% with a
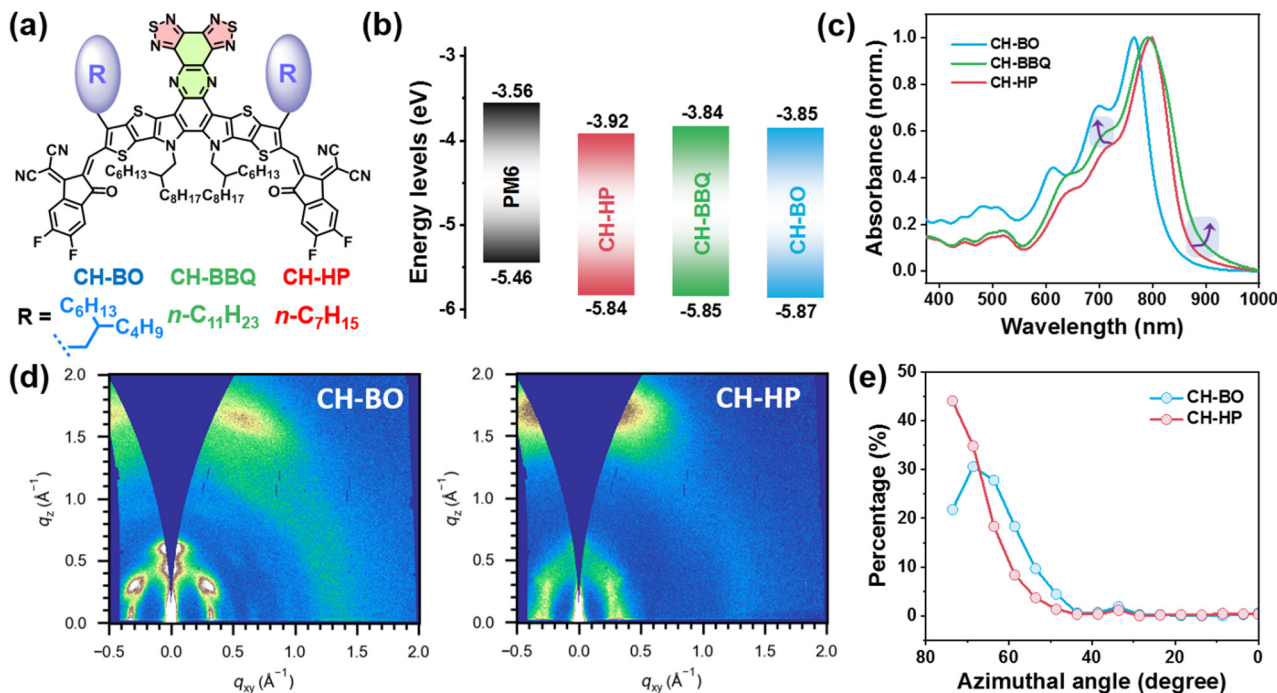
Fig. 1 (a) Molecular structure of acceptors. (b) Energy level diagram of PM6 and acceptors. (c) Normalized film absorption spectra of PM6 and acceptors. (d) 2D GIWAXS patterns of CH-BO and CH-HP based neat films; (e) the intensity azimuthal pole figure of (010) diffractions of CH-BO and CH-HP neat films.

satisfactory J_{SC} of 25.89 mA cm^{-2} and FF of over 80%, respectively. Moreover, with the addition of a guest acceptor BO-4Cl, a further enhanced PCE of 19.44% can be achieved using a PM6:CH-HP:BO-4Cl ternary system. To better understand the impact of the alkyl chain size on the donor/acceptor interactions and photovoltaic device performance, molecular dynamics (MD) simulation was performed. This work provides a new insight into the interaction between two main stacking motifs in NFAs, offers reference principles for the alkyl chain optimization of central extended NFAs, and suggests new guidelines (extended core plus shortened alkyl chains) for the molecular engineering of high-performance NFAs.

Results and discussion

The synthetic routes of CH-BO and CH-HP are displayed in Fig. S1 (ESI†). As key intermediates, diketones with different alkyl chains were firstly prepared, and fused-ring core units were constructed subsequently *via* a "diketone-diamine" condensation reaction; afterwards, formylation and the Knoevenagel condensation reaction were conducted, leading to the target acceptors. CH-BO and CH-HP exhibit excellent thermal stability with decomposition temperatures of 344 and 347 °C, respectively, as measured by thermal gravimetric analysis (TGA) (Fig. S6, ESI†). With sharing of the same π-conjugated backbone, the two new NFAs exhibit comparable high-lying highest occupied molecular orbital (HOMO) and LUMO energy levels with CH-BBQ, which make them energetically compatible with

the polymer donor PM6 (Fig. 1b and Fig. S2, ESI†). Similarly, all three NFAs show identical UV-vis absorption spectra (Fig. S3, ESI†) in diluted chloroform solution (*ca.* 3×10^{-6} mol L^{-1}). But their absorption spectra in thin films greatly differed (Fig. 1c). From CH-BBQ to CH-HP, the shortened linear alkyl chains result in a slightly red-shifted main absorption peak (from 791 nm to 799 nm), implying a closer intermolecular π–π stacking distance of CH-HP; in both short and long wavelength ranges, the absorption tail of CH-HP is better suppressed, suggesting the decreased localized states and reduced energetic disorder induced by the more ordered packing.[40] As to CH-BO, its main absorption peak merely redshifted *ca.* 45 nm from solution to films which is distinct from CH-HP (*ca.* 79 nm redshift) or L8-BO (*ca.* 76 nm redshift), suggesting its loosened packing mode in film potentially induced by the steric hindrance of the branched alkyl chain. The detailed physicochemical parameters are summarized in Table S1 (ESI†).

Grazing incidence wide-angle X-ray scattering GIWAXS measurements were also performed on neat films of CH-BO and CH-HP to extract quantified information of molecular packing. As shown in Fig. 1d and Fig. S17 (ESI†), the diffraction peak of π–π stacking (010) located in the OOP direction can be observed in the neat films of CH-BO and CH-HP, indicating that they both have a preferred "face-on" molecular orientation. However, it is noteworthy that over 44% of CH-HP crystallites displayed a π–π stacking signal at an azimuthal angle of around 74°, suggesting that a considerable ratio of molecules adopted the face-on orientation; in contrast, only 21% of CH-BO crystallites were arranged at the same angle (Fig. 1e). Moreover, the π–π
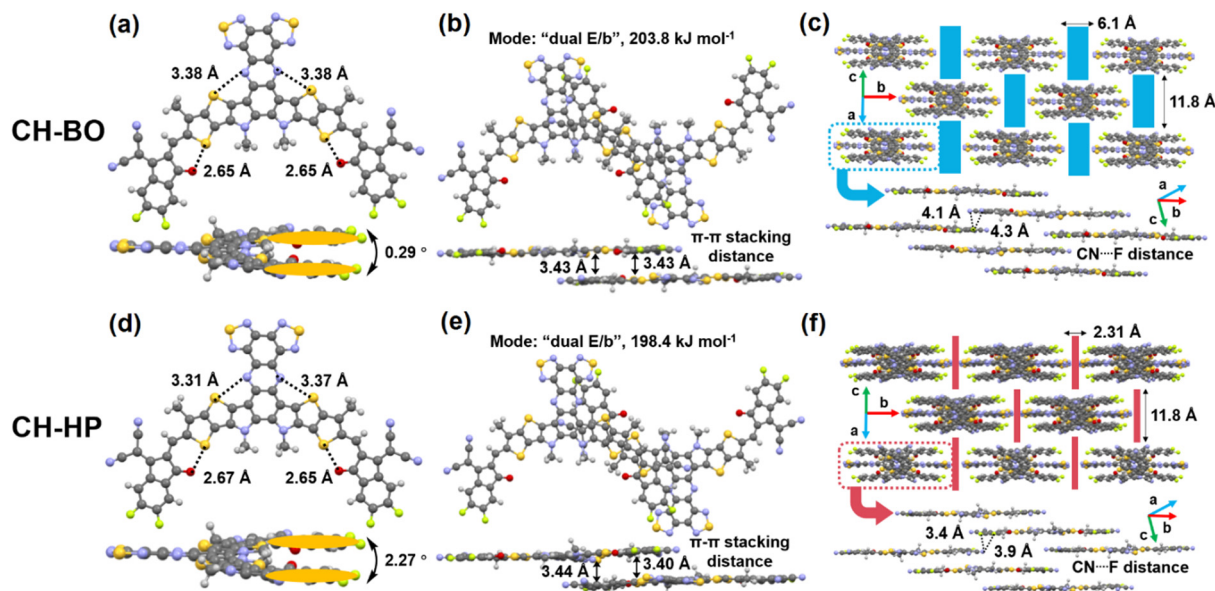
Fig. 2 (a) and (d) Monomolecular single crystallographic structure of CH-BO and CH-HP in the top- and side-view. The alkyl chains were represented by methyl groups for clarity. (b) and (e) π−π stacking distances of the interlayer with intermolecular packing modes of CH-BO and CH-HP. (c) and (f) Illustration of one-dimensional intermolecular packing and CN···F type interactions between neighbouring molecules in CH-BO and CH-HP.

stacking signal of the CH-HP crystallites concentrated in a narrower azimuthal angle range than that of CH-BO. Judging from the results above, it is inferable that CH-HP exhibits a stronger intermolecular interaction and more ordered intermolecular packing than CH-BO, which could be beneficial for carrier charge transport.[41,42]

To elucidate the preliminary results from spectroscopic measurements and clarify how the alkyl chain affects the packing modes of CH-BO and CH-HP, their single crystals were cultivated and analyzed accordingly. Single crystals can be successfully developed by diffusing methanol vapor into a chloroform solution. The molecular geometry and intermolecular packing pattern (all alkyl chains were omitted for clear presentation) in a single crystal of CH-BO and CH-HP (CCDC no. 2300122 and 2321689†) are exhibited in Fig. 2. As shown in Fig. 2a and d, both the acceptors present a banana-shaped configuration with potential intramolecular "S → N" and "S → O" noncovalent interactions and a slightly twisted conjugated backbone, which is similar to most Y-series and CH-series NFAs. However, distinct from most high-performance NFAs' single crystal with a three-dimensional π–π stacking network, both CH-BO and CH-HP display peculiar one-dimensional (1D) arrangements via a single intermolecular π–π stacking mode.

As shown in Fig. 2b and e, it can be found that the most common packing pattern of end-to-end units ("E/E") mode is missing; instead, only the "dual end to bridge units ("dual E/b") mode can be found in the CH-BO/CH-HP single crystal. A small π–π stacking distance of around 3.43 Å and a high intermolecular potential of around 200 kJ mol⁻¹ can be observed in this "dual E/b" packing mode, and through which CH-BO/CH-HP molecules form numerous 1D extended "molecular wires" that are mutually parallel but barely overlapped with each other. Despite sharing the same packing mode and monoclinic crystal system, the different alkyls still significantly affect the packing parameters of these two NFAs. As can be seen in Fig. 2c and f, the steric hindrance induced by 2-butyloctyl groups results in a much wider distance between the adjacent "molecular wires" in CH-BO crystals compared to that in CH-HP. This also leads to a higher crystal packing density, lower free volume, and a higher electron/hole transfer integral (Table 1) for CH-HP compared to that of CH-BO. Therefore, it can be estimated that CH-HP should be more favorable for efficient charge transport in devices.

The molecular packing not only affects the physiochemical properties, but also has a considerable impact on the intrinsic charge transport properties of NFA, which is pivotal for

Table 1 Crystallographic and π−π interaction parameters of CH-BO and CH-HP

Acceptor	Packing mode	$d_{\pi-\pi}$[a] (Å)	Intermolecular potential (kJ mol⁻¹)	V_E[b] (cm⁻¹)	V_E[c] (cm⁻¹)	Packing coefficient[d] (%)	Packing coefficient[e] (%)
CH-BO	Dual E/b	3.43	203.8	215.13	4.31	51.00	23.72
CH-HP	Dual E/b	3.44, 3.40	198.4	432.77	40.47	53.88	27.15

[a] π−π distance of the intermolecular packing mode of CH-BO and CH-HP. [b] Intra-stacking-chain electron transfer integral. [c] Inter-stacking-chain electron transfer integral. [d] Packing coefficient of single crystals. [e] Packing coefficient of single crystals with the conjugate fragment only.
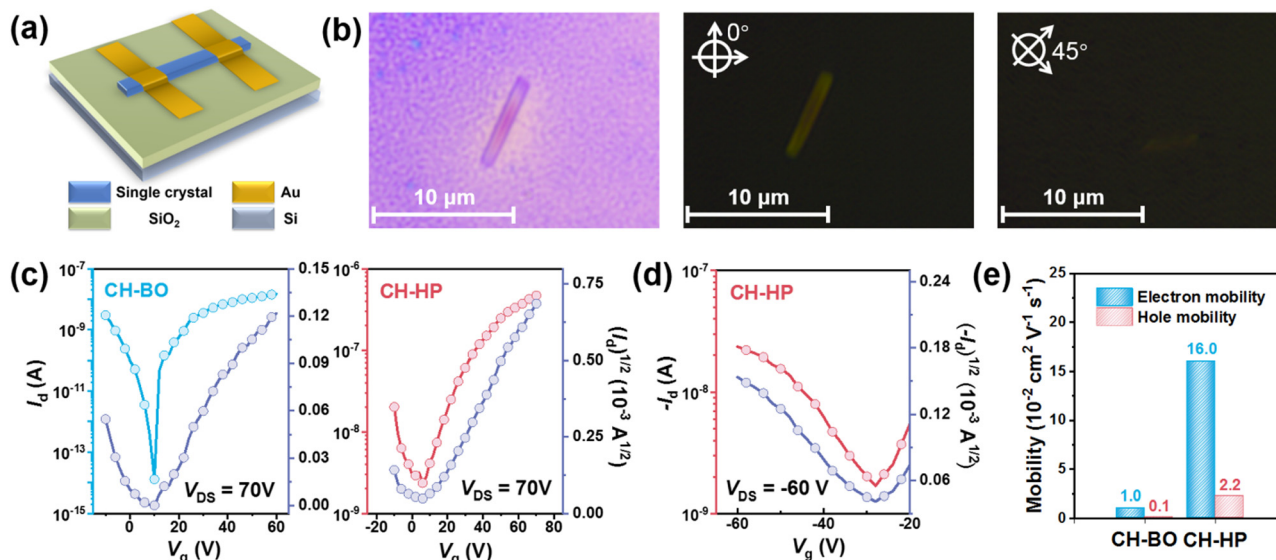
Fig. 3 (a) Architecture of the single-crystal OFET device. (b) Optical microscopy and polarized optical microscopy patterns of a single crystal of CH-HP prepared by drop-casting. (c) and (d) Transfer curves of OFET based on single crystals of CH-BO and CH-HP. (e) Carrier mobility diagram of the optimized devices.

achieving high performance OSC devices. To evaluate the capability of charge transport of these two NFAs, single-crystal OFET devices based on CH-BO and CH-HP were fabricated and characterized, respectively.[43–46] Single crystals of NFAs for devices were obtained *via* a drop-casting method, and the single-crystal orientation is proved by the strong birefringence in the polarized optical microscopy (POM) patterns (Fig. 3b). Then single crystal OFETs with a bottom-gate top-contact (BGTC) structure were fabricated (Fig. 3a) and were measured in a glove box under a nitrogen atmosphere. The details of measurement are described in the ESI.† As shown in Fig. 3c and d, both CH-HP and CH-BO demonstrated ambipolar charge transport characteristics. CH-BO exhibited an inferior electron mobility (μ_e) of 0.01 cm^2 V^{-1} s^{-1} and a negligible μ_h value (*ca.* 1.1 × 10^{-3} cm^2 V^{-1} s^{-1}); meanwhile, the CH-HP based device not only displays an essentially improved μ_e value of 0.16 cm^2 V^{-1} s^{-1} but also a decent μ_h value of 0.022 cm^2 V^{-1} s^{-1} which was even higher than the μ_e value of CH-BO and would facilitate the hole transport in BHJ films (Fig. 3e). This result verified that more ordered and compact molecular packing of CH-HP benefit charge transport.

The variated performance of OFETs based on CH-BO and CH-HP revealed significant distinctions in their intrinsic capabilities of charge carrier transport, which drove us to

further explore their photovoltaic properties in OSC devices. The OSCs based on CH-BO and CH-HP were fabricated and characterized. A conventional BHJ device with the architecture of ITO/PEDOT:PSS/active blend/PNDIT-F3N/Ag was adopted, and PM6 was used as a polymer donor. Despite exhibiting a high V_{OC} value of up to 0.984 V, CH-BO based OSCs exhibited low J_{SC} and FF values of 17.46 mA cm^{-2} and 66.9%, respectively, and consequently a mediocre PCE of 11.43% (Table 2). Meanwhile, CH-HP based devices demonstrated satisfactory performance. Compared with CH-BO, an essentially improved PCE of 18.74% was obtained along with a V_{OC} of 0.903 V, a J_{SC} of 25.89 mA cm^{-2} and a FF of up to 80.1%. In addition, despite exhibiting a slightly reduced J_{SC} value due to the narrower absorption of CH-HP, the elevated V_{OC} and FF values of PM6:CH-HP binary make it outperform those of PM6:CH-BBQ. It is noteworthy that a unique anti-correlation effect of the alkyl chain size on the photovoltaic performance was observed in this centrally extended NFAs which differs from most previously reported cases,[47,48] suggesting the new design rule (extended central core with a shortened alkyl chain) for NFAs. Moreover, after introducing a second NFA BO-4Cl as a guest component to construct ternary OSCs with an extended EQE response, the J_{SC} experienced another enhancement and an impressively high PCE of 19.44% was achieved with a

Table 2 Photovoltaic parameters of best devices (PM6 as a polymer donor)[a]

BHJs	V_{OC} (V)	J_{SC} (mA cm^{-2})	FF (%)	PCE (%)	Calc. J_{SC}[b] (mA cm^{-2})
PM6:CH-BO	0.984 (0.982 ± 0.003)	17.46 (17.30 ± 0.16)	66.9 (66.5 ± 0.5)	11.43 (11.40 ± 0.03)	16.75
PM6:CH-BBQ	0.881 (0.877 ± 0.003)	26.15 (26.12 ± 0.26)	78.9 (78.8 ± 0.3)	18.19 (18.04 ± 0.12)	25.21
PM6:CH-HP	0.903 (0.902 ± 0.002)	25.89 (25.65 ± 0.25)	80.1 (79.8 ± 0.3)	18.74 (18.71 ± 0.03)	24.95
PM6:CH-HP:BO-4Cl	0.885 (0.886 ± 0.003)	27.97 (27.79 ± 0.19)	78.5 (78.1 ± 0.4)	19.44 (19.39 ± 0.05)	26.87

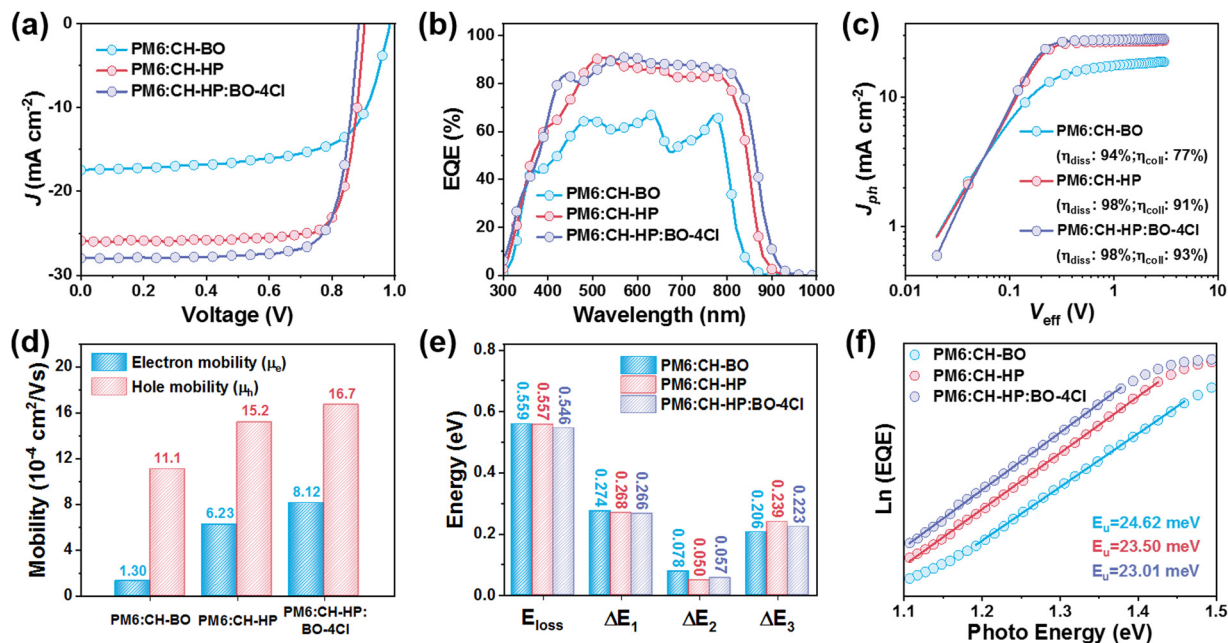[a] The average parameters were calculated from 15 independent devices. [b] Current densities calculated from EQE curves.

Fig. 4 (a) Current density–voltage (*J*–*V*) characteristics and (b) external quantum efficiency curves of the optimized devices. (c) Exciton dissociation/charge collection efficiencies of the optimized devices. (d) Mobility diagram for the optimized devices. (e) E_{loss} diagram for the optimized devices. (f) Urbach energy of binary/ternary devices.

V_{OC} value of 0.885 V, a J_{SC} value of 27.97 mA cm^{-2} and a FF of 78.5%.

Besides physiochemical properties and molecular packing of NFAs, the charge carrier dynamics and morphology of photoactive blend films also play pivotal roles in OSC devices. Therefore, charge carrier dynamics in OSCs were investigated. As displayed in Fig. 4c, CH-BO based OSCs suffered inferior exciton dissociation efficiency (η_{diss}, 94%) and charge collection efficiency (η_{coll}, 77%); meanwhile, CH-HP based devices show higher η_{diss} values of over 98% and η_{coll} values of over 91% which is indisputably beneficial for the improvement of J_{SC} and EQE. The higher η_{coll} values are usually attributed to the higher hole/electron mobility (μ_h, μ_e) and more balanced μ_h/μ_e values of BHJ blends. Therefore, the hole/electron-transport only diodes were fabricated to evaluate the charge transport properties of BHJs. Consistent with the data from OFET devices, PM6:CH-BO blends exhibited hole/electron mobilities of $11.1 \times 10^{-4}/1.3 \times 10^{-4}$ cm^2 V^{-1} s^{-1} (μ_h/μ_e ratio of 8.53) while PM:CH-HP blends show not only higher hole/electron mobilities ($15.2 \times 10^{-4}/6.23 \times 10^{-4}$ cm^2 V^{-1} s^{-1}) but also a more balanced μ_h/μ_e ratio (2.44) (Fig. 4d, Fig. S12 and Table S9, ESI†). To probe two major charge recombination channels that cause the loss of FFs and PCEs, bimolecular recombination and trap-assisted recombination in OSC devices were quantified. From the dependence of J_{SC} and V_{OC} on the light intensity, the bimolecular recombination is unlikely to have a major impact on all three binary OSCs, and trap-assisted recombination was the major recombination channel in devices of PM6:CH-BO and PM6:CH-HP (Fig. S13 and Table S10, ESI†). In addition, transient photocurrent/photovoltage (TPC/TPV) measurements were also conducted to quantitatively analyse the charge

recombination/extraction process in OSC devices. As shown in Fig. S14 (ESI†), CH-HP based devices not only demonstrated a faster charge extraction time (0.45 μs) but also a longer carrier lifetime (18.25 μs) than those of CH-BO based devices.

The total energy loss (E_{loss}) of OSCs of binary/ternary OSCs was analyzed by using the following equation:[49]

$$E_{loss} = E_g^{PV} - qV_{OC} = (E_g^{PV} - qV_{OC}^{SQ}) + (qV_{OC}^{SQ} - qV_{OC}^{rad})$$
$$+ (qV_{OC}^{rad} - qV_{OC}) = \Delta E_1 + \Delta E_2 + \Delta E_3$$

As shown in Fig. 4e, the alkyl chain variation has a marginal impact on ΔE_1 in optimized OSC devices. As to ΔE_2, which originated from radiative recombination below the bandgap, can be alleviated by reducing the energy level offset between the donor and the acceptor. Consequently, the CH-HP based OSCs display a lower ΔE_2 of 0.050 eV than CH-BO (0.078 eV) owing to its shallower HOMO energy level. The ΔE_3 values were calculated by using two different methods and exhibited a consistent trend. The binary device based on PM6:CH-BO yielded the highest EQE$_{EL}$ of 1.49×10^{-4} which leads to the smallest ΔE_3 of 0.206 eV. Finally, the total E_{loss} values were quantified as 0.559, 0.557 and 0.546 eV for CH-BO/CH-HP based binary and CH-HP based ternary devices, respectively (see details in the ESI,† Section S12, Fig. S11 and Table S8). Furthermore, Fourier transform photocurrent spectroscopy-external quantum efficiency (FTPS-EQE) was measured to evaluate the Urbach energy in different binary/ternary systems. Consistent with the results of E_{loss} analysis, the CH-HP based binary device exhibited a smaller Urbach energy (E_u) of 23.50 meV compared with that of the CH-BO based binary system of 24.63 meV, indicating smaller energetic disorder caused by more ordered

intermolecular packing of PM6:CH-HP; The formation of the ternary system further reduces E_u to 23.01 meV.

The blend film morphology plays a crucial role in achieving favorable charge carrier dynamics and PCE recorded in OSCs.[50] Therefore, the grazing-incidence wide-angle X-ray scattering (GIWAXS) technique and atomic force microscopy (AFM) were employed to probe donor/acceptor molecular packing behaviors and phase separation in thin films. In D:A blends, the d-spacings and corresponding CLs of the (010) peak are estimated to be 3.62 and 16.2 Å for PM6:CH-BO and 3.65 and 16.3 Å for PM6:CH-HP (Fig. 5a, b and Fig. S17, Table S13, ESI†), indicating similar intermolecular packing and crystallinity of two binary systems. The AFM images also illustrate that both the blend films present fiber-like and uniform surfaces along with good phase separation, and the root mean square (RMS) roughness values of PM6:CH-BO and PM6:CH-HP are 3.80 and 3.29 nm (Fig. S16, ESI†), respectively. The data above obtained from those rudimentary morphological characterization studies seem inadequate for explaining the substantial performance differences between the two binary systems. Therefore, atomic force microscopy-based infrared spectroscopy (AFM-IR) was further used to extract more information from the fibril structure in two binary blends, using a specific IR absorption at 2216 cm^{-1} for CH-BO/CH-HP. As shown in Fig. 5d and e, in PM6:CH-BO blends, only the continuous network of CH-BO can be observed. The polymer donor was dispersed into very small domains and enveloped by the acceptor domain, unable to provide sufficient donor/acceptor interfaces and continuous channels for efficient charge transport, which leads to the inferior FF and J_{SC} values of PM6:CH-BO. In contrast, a typical bicontinuous interpenetrating network was formed in PM6:CH-HP blends, benefitting exciton dissociation and charge transport.[51] The favorable D–A interfacial interactions in PM6:CH-HP blends were also evidenced by their much higher photoluminescence quenching efficiencies (η_{PLQ}) compared with those of PM6:CH-BO, as presented in Fig. S5 and Table S2 (ESI†).

The above-mentioned experimental data indicate that the size of the alkyl chain considerably impacts the intrinsic packing density and charge carrier transport of the sole centrally extended NFAs. However, despite the characterization results (photovoltaic performance, charge carrier dynamic parameters, blend film dielectric constant, *etc.*) confirming that the size of the alkyl chain also exerts a profound influence on the donor/acceptor interaction, the existing morphological tests hardly provide a more straightforward understanding of the differences in interaction modes between the two sets of donor/acceptor, as well as the distinctions in exciton and charge carrier behaviors at the donor/acceptor interface. For an in-depth study on how the side chains cause substantial differences in this case and to shed light on further molecular optimization of NFAs, molecular dynamics (MD) simulations were conducted to explore the D–A interactions at the molecular level. 90 NFA molecules and 15 8-mers of PM6 were introduced into the simulation box. The system was first subjected to annealing and equilibration simulations for 20 ns, followed by a production run for 60 ns. Five replicate simulations were performed for each of the two systems under investigation. The final 50 ns of the ten production trajectories were utilized to analyse the stacking between conjugated segments. A pair of non-hydrogen atoms that resided closer than 3.6 Å on different conjugated segments were defined as a close contact. If there were more than two such contacts between two segments, the segments were considered to have stacking interactions.

Based on the stacking interactions occurring around an NFA molecule with other molecules, NFA molecules were categorized into five distinct groups, as shown in Fig. 6c. Type D0A1 NFAs are defined by their lack of stacking interactions with polymer donors, instead exhibiting stacking exclusively with another NFA molecule. These NFAs can be regarded as dead ends for electron transfer, which is not desirable. Type DnA0 refers to those NFA molecules that stack with one or more
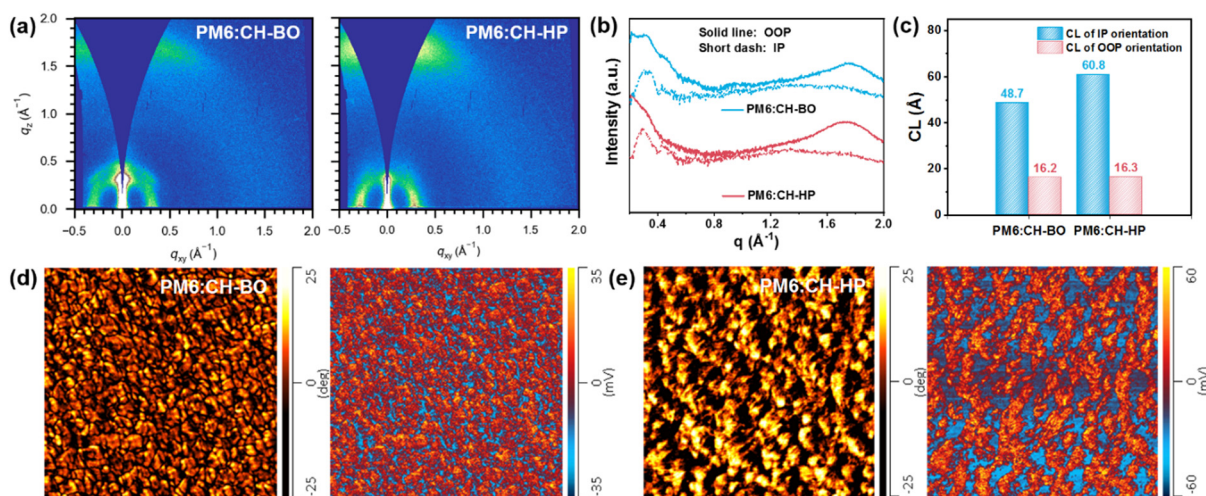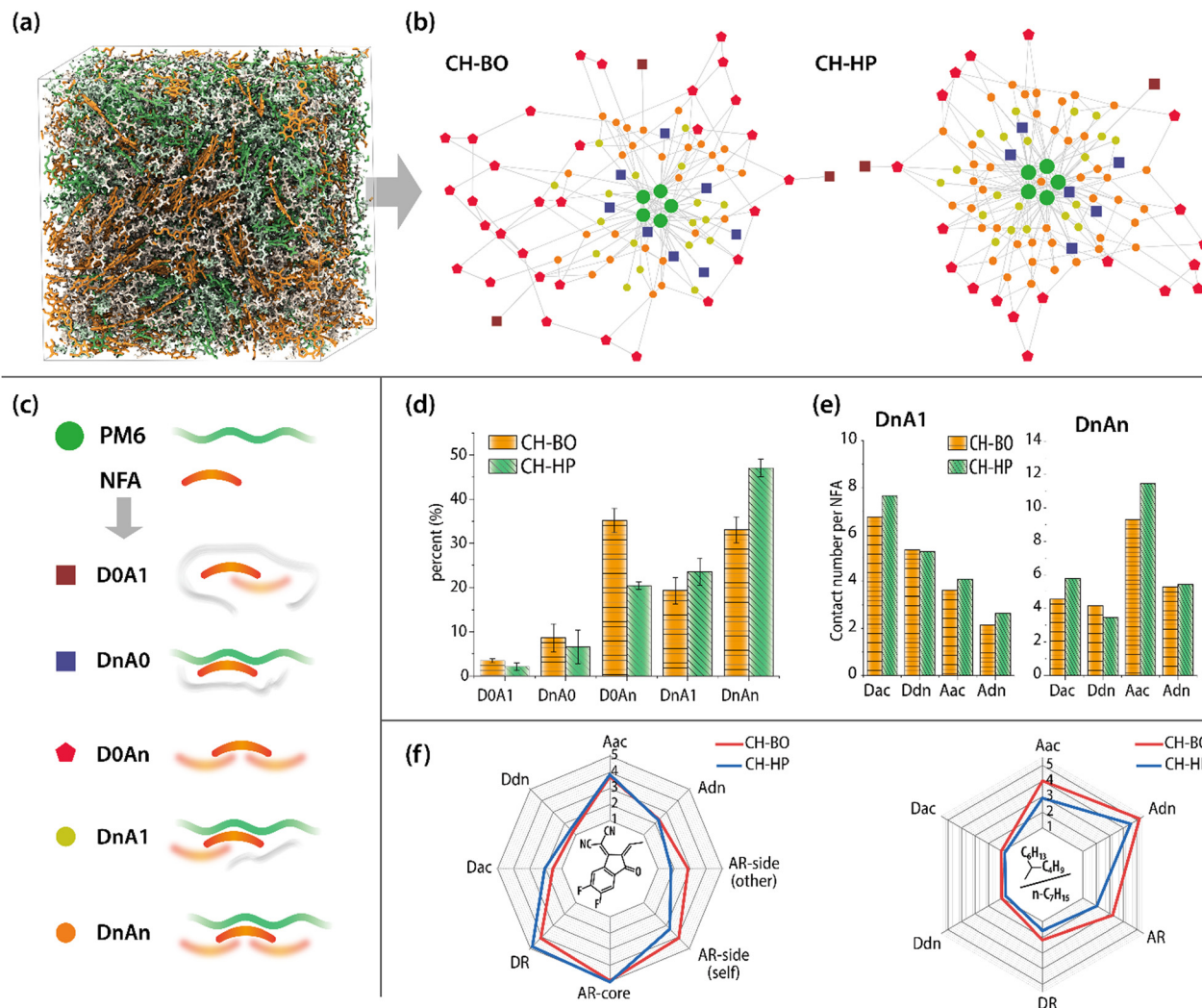

Fig. 5 Morphology characterization of relevant blend films. (a) 2D GIWAXS patterns and (b) in-plane/out-of-plane line-cut profiles of blend films; (c) coherence length diagram of binary blends; (d) and (e) tapping AFM-IR image at a wavenumber of 2216 cm^{-1} of the optimized binary blends.

Fig. 6 (a) A snapshot from the MD trajectory of the PM6:CH-HP system. Green represents the PM6 backbone, orange represents the CH-HP backbone, and light green and white represent alkyl chains in PM6 and CH-HP, respectively. (b) Stacking topology graphs generated from the molecular stacking in the MD trajectory. Green nodes represent the 24-mer of PM6, whereas other shapes represent an NFA molecule situated in a unique stacking environment, with specific correspondences illustrated in (c). Edges depict the stacking interactions between two molecules. (c) An illustration classifying NFA based on the stacking environment with neighboring molecules. (d) The proportion of various stacking states of NFA in the two systems. (e) For NFAs in the DnA1 and DnAn stacking environments, the interaction strengths with other fragments were quantified in terms of contact numbers, defined as a pair of non-hydrogen atoms from different conjugated segments within a distance of 3.6 Å being considered as one contact. On the horizontal axis, Dac represents the acceptor segments of PM6, Ddn represents the donor segments of PM6, Aac represents the acceptor segments of the NFA molecule, and Adn represents the donor segments of the NFA molecule. (f) The left diagram shows an analysis of the Aac group's neighbouring atoms, defined as non-hydrogen atoms from other groups within 3.6 angstroms of Aac's non-hydrogen atoms or hydrogen atoms within 3.0 angstroms. The radar chart measures the count of neighbouring atoms from various groups: 'DR' for alkyl chains on the donor polymer, 'AR-core' for *N*-alkyl chains on NFAs, 'AR-side' for side alkyl chains on NFAs, 'other' for atoms from another molecule, and 'self' for atoms from the same molecule. The right diagram features the AR-side group's neighbouring atom analysis. Here, neighbours are non-hydrogen atoms within 3.0 angstroms of AR-side's hydrogen atoms or hydrogen atoms within 2.4 angstroms from other groups.

polymers but without any other NFAs. This implies that the electrons generated at the D–A interface cannot be transferred into the acceptor phase, thus marking this as an unfavorable stacking environment for NFA. Type D0An represents NFAs that do not stack with polymers but do stack with two or more other NFA molecules, identifying them as NFA molecules in a pure acceptor phase. DnA1s are NFAs that stack with one or more polymer chains and pair up with another NFA. In contrast, DnAn NFAs not only stack with multiple polymers but they also

interact with two or more NFAs. Both DnA1 and DnAn types are crucial components of the material's interface, with DnAn additionally enhancing electron transport. These NFAs are considered to be the most advantageous. Subsequently, the stacking interactions among all conjugated segments within the system were calculated, leading to the construction of a topological diagram of the stacking patterns, depicted in Fig. 6b. In this diagram, polymer chains are represented by green nodes. Owing to the extensive stacking between polymer

chains, fifteen octamers were simplified into five 24-mers for a clearer representation. Other nodes signify the various stacking environments of NFA mentioned earlier, whereas rectangular nodes denote the unfavorable D0A1 and DnA0 types of acceptors. It is observable that these two sorts of nodes are less numerous in the PM6:CH-HP system. The pentagon-shaped red nodes in the diagram symbolize NFAs that are in a pure acceptor phase, with a noticeably higher proportion of such NFAs present in the PM6:CH-BO system. However, the CH-HP:PM6 system does not necessarily have fewer electron transport pathways; it actually features a significantly higher number of DnAn-type NFAs, which are capable of both dissociating excitons and facilitating electron transport. The proportions of these five types of NFAs are quantitatively displayed in Fig. 6d.

Furthermore, regarding the interfacial NFAs of types DnA1 and DnAn, a comparison was made of their interaction strengths with different segments in two binary systems. The PM6:CH-HP system shows a substantial increase in interaction strength with the acceptor segments of PM6 (Dac), which favors the occurrence of charge separation. In contrast, interactions with the donor segments of PM6 (Ddn) show a slight decrease, aiding in suppressing charge recombination. Additionally, the interactions of CH-HP with both donor and acceptor segments of NFA (Aac, Adn) are enhanced, with the acceptor segments (Aac) showing more significant strengthening. This further benefits the transfer of electrons between NFAs in the PM6:CH-HP system.

To provide a clearer understanding of the role played by 2-butyloctyl (BO) or n-heptyl (HP) groups in molecular packing, a neighbor atom analysis was conducted on the trajectories. Fig. 6f (left panel) illustrates the average composition of neighboring atoms around the Aac groups in all NFA molecules. The spatial vicinity of Aac groups is predominantly occupied by alkyl chains, with interactions extending to other NFA molecules' acceptor and donor groups. Conversely, there are fewer interactions with the conjugated segments of the polymer. Upon replacing the BO (AR-side) with HP on NFAs, there is a noticeable reduction in the number of AR-side atoms from the self and other NFAs within the Aac's neighboring space. The vacated space is mainly occupied by the polymer's alkyl chains (DR) and their acceptor groups (Dac), with a slight increase in the atoms of adjacent acceptor segments (Aac) of other NFA molecules, which undoubtedly facilitates charge separation and electron transport. This not only confirms why HP increases the concentration of NFAs at the interface, but also suggests that the decrease of D0An-type acceptors due to HP does not compromise electron transport, as each Aac segment is surrounded by more Aac. Illustrated on the right panel of Fig. 6f is the average neighbor atom composition for the BO or HP groups of all NFA molecules. The neighboring space of the alkyl chains on the acceptor is predominantly occupied by the donor units (Adn) of the acceptor, followed by the acceptor's acceptor units (Aac) and the alkyl chains on the acceptor (AR), while there is relatively weak interaction with donor conjugate units. The transition of alkyl chains from HP to BO results in an increase in all categories of neighboring atoms due to BO's greater surface area, accommodating more atoms. Nonetheless,

it is observed that replacing HP with BO mainly results in larger numbers of NFA neighbors rather than polymer donors, suggesting that more sizable alkyl chains acting alongside a central extended Adn unit can synergistically enhance the intermolecular forces among NFAs, leading to a reduced presence of NFA molecules at the interface. This would decrease exciton separation, while the strong interaction of large side alkyl chains and the central cores could reinforce the shielding of the conjugated unit. This weakens the stacking of conjugated segments, subsequently lower than the intraphase carrier mobility within the acceptor phase. Notably, Zhu *et al.* recently reported a series of acceptors featured with a fluorinated quinoxaline core.[52] In this case, the acceptor AQx-2F with BO side chains achieved an impressively high efficiency of 19.7% in binary devices. Combining these results with our data, it can be seen that the compromise of the size of the central core and side chains is essential to achieve optimal performance in the corresponding acceptors.[53]

In summary, compared to the PM6:CH-BO system, the PM6:CH-HP system exhibits fewer unfavorable NFAs, more multifunctional NFAs at the interface and a better and stronger stacking arrangement between NFAs and polymers. These factors collectively contribute to enhanced exciton separation, reduced exciton recombination, and improved electron transport. The possible reason for the inferior performance of CH-BO could be that the coexistence of the centrally extended core and sizable alkyl chains leads to intensive inter- and intramolecular alkyl chain–π interactions. This not only hinders nano-sized phase separation, but also interferes with the electron transfer within the NFA phases.

Conclusions

In this work, the size effect of the alkyl chain on the photovoltaic performance of centrally extended NFAs was systematically investigated. Different from the 3D packing mode of Y-series NFAs, benzobisthiadiazole embedded NFAs exhibit an unusual 1D packing mode in single crystals. Therefore, introducing sizable 2-butyloctyl groups results in unexpected negative effects distinctive to previous reports: including blue-shifted absorption, loosened crystal packing, and inferior charge carrier mobility of the corresponding NFA CH-BO; in contrast, n-heptyl substituted CH-HP exhibited more compact molecular packing and superior charge transport capability. More importantly, the PM6:CH-HP blends exhibit enhanced dielectric constant, more favorable phase separation, and more optimized charge carrier dynamics compared to PM6:CH-BO blends. MD simulation results indicate that the more sizable alkyl chains of CH-BO hinder its effective intermolecular packing with PM6 and itself, impeding efficient exciton dissociation/diffusion and charge carrier transport at the donor/acceptor interfaces. Consequently, OSC devices based on CH-HP achieved a high efficiency of 18.74% (19.44% for ternary devices), outperforming CH-BO based systems (11.43% for binary devices). This peculiar anti-correlation effect provides a

new perspective to examine the relationship between alkyl chains and central cores, along with their synergistic impact on NFA performance. In addition, the 1D crystal stacking of CH-HP implied that compared to the self-stacking pattern of the NFA molecules, their effective stacking with donor molecules might be more crucial for achieving satisfactory device performance.

Author contributions

T. Duan, C. Zhong, Y. Zhao, B. Kan and Y. Chen designed the work plan for this research; T. Duan, X. Bi, Y. Long and K. Tu contributed to the material design and synthesis; X. Zuo and X. Bi cultivated single crystals of CH-BO and CH-HP, and performed the single crystal XRD analysis; T. Duan, X. Bi and W. Chao performed UV-vis, CV, TGA, DSC and contact angle measurements; J. Wang and Y. Li fabricated and optimized the devices, and performed charge recombination, TPC/TPV, SCLC measurements and E_{loss} analysis; X. Zuo fabricated and characterized single-crystal OFET devices; J. Wang, K. Yang, H. Zhou and X. Wan performed the morphology characterization and analysis; C. Zhong conducted the DFT calculation, MD simulation and data analysis. T. Duan and B. Kan wrote the draft manuscript, and all the authors contributed to the revision of the manuscript. Y. Chen mentored the other authors throughout the whole research.

Data availability

The data that support the findings of this study are available in the ESI† of this article.

Conflicts of interest

The authors declare no conflicts of interest.

Acknowledgements

Notes and references

1 H. Zhang, C. Tian, Z. Zhang, M. Xie, J. Zhang, L. Zhu and Z. Wei, *Nat. Commun.*, 2023, **14**, 6312.

2 H. Xia, Y. Zhang, K. Liu, W. Deng, M. Zhu, H. Tan, P. W. K. Fong, H. Liu, X. Xia, M. Zhang, T. A. Dela Peña, R. Ma, M. Li, J. Wu, Y. Lang, J. Fu, W.-Y. Wong, X. Lu, W. Zhu and G. Li, *Energy Environ. Sci.*, 2023, **16**, 6078–6093.

3 Y. Xu, J. Wang, T. Zhang, Z. Chen, K. Xian, Z. Li, Y.-H. Luo, L. Ye, X. Hao, H. Yao and J. Hou, *Energy Environ. Sci.*, 2023, **16**, 5863–5870.

4 Y. Cai, Q. Li, G. Lu, H. S. Ryu, Y. Li, H. Jin, Z. Chen, Z. Tang, G. Lu, X. Hao, H. Y. Woo, C. Zhang and Y. Sun, *Nat. Commun.*, 2022, **13**, 2369.

5 Y. Lin, J. Wang, Z. G. Zhang, H. Bai, Y. Li, D. Zhu and X. Zhan, *Adv. Mater.*, 2015, **27**, 1170–1174.

6 J. Yuan, Y. Zhang, L. Zhou, G. Zhang, H.-L. Yip, T.-K. Lau, X. Lu, C. Zhu, H. Peng, P. A. Johnson, M. Leclerc, Y. Cao, J. Ulanski, Y. Li and Y. Zou, *Joule*, 2019, **3**, 1140–1151.

7 R. Zeng, L. Zhu, M. Zhang, W. Zhong, G. Zhou, J. Zhuang, T. Hao, Z. Zhou, L. Zhou, N. Hartmann, X. Xue, H. Jing, F. Han, Y. Bai, H. Wu, Z. Tang, Y. Zou, H. Zhu, C. C. Chen, Y. Zhang and F. Liu, *Nat. Commun.*, 2023, **14**, 4148.

8 S. Luo, C. Li, J. Zhang, X. Zou, H. Zhao, K. Ding, H. Huang, J. Song, J. Yi, H. Yu, K. S. Wong, G. Zhang, H. Ade, W. Ma, H. Hu, Y. Sun and H. Yan, *Nat. Commun.*, 2023, **14**, 6964.

9 L. Zhu, M. Zhang, J. Xu, C. Li, J. Yan, G. Zhou, W. Zhong, T. Hao, J. Song, X. Xue, Z. Zhou, R. Zeng, H. Zhu, C. C. Chen, R. C. I. MacKenzie, Y. Zou, J. Nelson, Y. Zhang, Y. Sun and F. Liu, *Nat. Mater.*, 2022, **21**, 656–663.

10 K. Jiang, J. Zhang, C. Zhong, F. R. Lin, F. Qi, Q. Li, Z. Peng, W. Kaminsky, S.-H. Jang, J. Yu, X. Deng, H. Hu, D. Shen, F. Gao, H. Ade, M. Xiao, C. Zhang and A. K. Y. Jen, *Nat. Energy*, 2022, **7**, 1076–1086.

11 L. Meng, H. Liang, G. Song, M. Li, Y. Huang, C. Jiang, K. Zhang, F. Huang, Z. Yao, C. Li, X. Wan and Y. Chen, *Sci. China Chem.*, 2023, **66**, 808–815.

12 X. Wu, X. Jiang, X. Li, J. Zhang, K. Ding, H. Zhuo, J. Guo, J. Li, L. Meng, H. Ade and Y. Li, *Adv. Mater.*, 2023, **35**, 2302946.

13 H. Lai, H. Chen, Z.-Y. Chen, Y. Lang, Y. Zhu, S.-T. Zhang, X. Lai, P. Tan, Y. Zhang, B. Yang, G. Li and F. He, *Energy Environ. Sci.*, 2023, **16**, 5944–5955.

14 F. Zhao, C. Wang and X. Zhan, *Adv. Energy Mater.*, 2018, **8**, 1703147.

15 G. Han, Y. Yi and Z. Shuai, *Adv. Energy Mater.*, 2018, **8**, 1702743.

16 Y. Shi, Y. Chang, K. Lu, Z. Chen, J. Zhang, Y. Yan, D. Qiu, Y. Liu, M. A. Adil, W. Ma, X. Hao, L. Zhu and Z. Wei, *Nat. Commun.*, 2022, **13**, 3256.

17 L. Ye, K. Weng, J. Xu, X. Du, S. Chandrabose, K. Chen, J. Zhou, G. Han, S. Tan, Z. Xie, Y. Yi, N. Li, F. Liu, J. M. Hodgkiss, C. J. Brabec and Y. Sun, *Nat. Commun.*, 2020, **11**, 6005.

18 W. Wei, X. Zhou, S. Pang, J. Zhou, X. Yuan, J. Li, Y. Chen, L. Pan, Z. Xie, H. Wu, F. Huang, Y. Cao and C. Duan, *Aggregate*, 2024, e488, DOI: 10.1002/agt2.488.

19 H. Chen, Y. Zou, H. Liang, T. He, X. Xu, Y. Zhang, Z. Ma, J. Wang, M. Zhang, Q. Li, C. Li, G. Long, X. Wan, Z. Yao and Y. Chen, *Sci. China Chem.*, 2022, **65**, 1362–1373.

20 Y. Zou, H. Chen, X. Bi, X. Xu, H. Wang, M. Lin, Z. Ma, M. Zhang, C. Li, X. Wan, G. Long, Y. Zhaoyang and Y. Chen, *Energy Environ. Sci.*, 2022, **15**, 3519–3533.

21 Z. Zhong, S. Chen, J. Zhao, J. Xie, K. Zhang, T. Jia, C. Zhu, J. Jing, Y. Liang, L. Hong, S. Zhu, D. Ma and F. Huang, *Adv. Energy Mater.*, 2023, **13**, 2302273.

22 B. Zhou, L. Wang, Y. Liu, C. Guo, D. Li, J. Cai, Y. Fu, C. Chen, D. Liu, Y. Zhou, W. Li and T. Wang, *Adv. Funct. Mater.*, 2022, **32**, 2206042.

23 Z. Luo, T. Xu, C. Zhang and C. Yang, *Energy Environ. Sci.*, 2023, **16**, 2732–2758.

24 J. Shi, Z. Chen, Y. Qiu, M. Luo, X. Zhang and Z. Ge, *Sol. RRL*, 2023, **7**, 2300206.

25 C. Xiao, X. Wang, T. Zhong, R. Zhou, X. Zheng, Y. Liu, T. Hu, Y. Luo, F. Sun, B. Xiao, Z. Liu, C. Yang and R. Yang, *Adv. Sci.*, 2023, **10**, 2206580.

26 Y. Guo, Z. Chen, J. Ge, J. Zhang, L. Xie, R. Peng, W. Ma and Z. Ge, *Sci. China Chem.*, 2023, **66**, 500–507.

27 N. Li and C. J. Brabec, *Sci. China Chem.*, 2021, **64**, 1435–1436.

28 J. Song, L. Zhu, C. Li, J. Xu, H. Wu, X. Zhang, Y. Zhang, Z. Tang, F. Liu and Y. Sun, *Matter*, 2021, **4**, 2542–2552.

29 W. Zhong, M. Zhang, L. Zhu, Y. Zhang and F. Liu, *Trends Chem.*, 2022, **4**, 699–713.

30 H. Chen, H. Liang, Z. Guo, Y. Zhu, Z. Zhang, Z. Li, X. Cao, H. Wang, W. Feng, Y. Zou, L. Meng, X. Xu, B. Kan, C. Li, Z. Yao, X. Wan, Z. Ma and Y. Chen, *Angew. Chem., Int. Ed.*, 2022, **61**, e202209580.

31 H. Liang, X. Bi, H. Chen, T. He, Y. Lin, Y. Zhang, K. Ma, W. Feng, Z. Ma, G. Long, C. Li, B. Kan, H. Zhang, O. A. Rakitin, X. Wan, Z. Yao and Y. Chen, *Nat. Commun.*, 2023, **14**, 4707.

32 H. Chen, B. Kan, P. Wang, W. Feng, L. Li, S. Zhang, T. Chen, Y. Yang, T. Duan, Z. Yao, C. Li, X. Wan and Y. Chen, *Angew. Chem., Int. Ed.*, 2023, **62**, e202307962.

33 Z. Yao, X. Wan, C. Li and Y. Chen, *Acc. Mater. Res.*, 2023, **4**, 772–785.

34 H. Chen, Z. Zhang, P. Wang, Y. Zhang, K. Ma, Y. Lin, T. Duan, T. He, Z. Ma, G. Long, C. Li, B. Kan, Z. Yao, X. Wan and Y. Chen, *Energy Environ. Sci.*, 2023, **16**, 1773–1782.

35 K. Liu, Y. Jiang, F. Liu, G. Ran, F. Huang, W. Wang, W. Zhang, C. Zhang, J. Hou and X. Zhu, *Adv. Mater.*, 2023, **35**, 2300363.

36 Z. Yao, X. Cao, X. Bi, T. He, Y. Li, X. Jia, H. Liang, Y. Guo, G. Long, B. Kan, C. Li, X. Wan and Y. Chen, *Angew. Chem., Int. Ed.*, 2023, **62**, e202312630.

37 Y. Jiang, Y. Li, F. Liu, W. Wang, W. Su, W. Liu, S. Liu, W. Zhang, J. Hou, S. Xu, Y. Yi and X. Zhu, *Nat. Commun.*, 2023, **14**, 5079.

38 F. Liu, L. Zhou, W. Liu, Z. Zhou, Q. Yue, W. Zheng, R. Sun, W. Liu, S. Xu, H. Fan, L. Feng, Y. Yi, W. Zhang and X. Zhu, *Adv. Mater.*, 2021, **33**, 2100830.

39 T. Duan, W. Feng, Y. Li, Z. Li, Z. Zhang, H. Liang, H. Chen, C. Zhong, S. Jeong, C. Yang, S. Chen, S. Lu, O. A. Rakitin, C. Li, X. Wan, B. Kan and Y. Chen, *Angew. Chem., Int. Ed.*, 2023, **62**, e202308832.

40 Y. Cui, H. Yao, J. Zhang, K. Xian, T. Zhang, L. Hong, Y. Wang, Y. Xu, K. Ma, C. An, C. He, Z. Wei, F. Gao and J. Hou, *Adv. Mater.*, 2020, **32**, 1908205.

41 H. Chen, D. Hu, Q. Yang, J. Gao, J. Fu, K. Yang, H. He, S. Chen, Z. Kan, T. Duan, C. Yang, J. Ouyang, Z. Xiao, K. Sun and S. Lu, *Joule*, 2019, **3**, 3034–3047.

42 N. Kim, B. H. Lee, D. Choi, G. Kim, H. Kim, J.-R. Kim, J. Lee, Y. H. Kahng and K. Lee, *Phys. Rev. Lett.*, 2012, **109**, 106405.

43 Z. Wu, W. Liu, X. Yang, W. Li, L. Zhao, K. Chi, X. Xiao, Y. Yan, W. Zeng, Y. Liu, H. Chen and Y. Zhao, *Angew. Chem., Int. Ed.*, 2023, **62**, e202307695.

44 Y. Chen, Z. Wu, L. Ding, S. Zhang, Z. Chen, W. Li, Y. Zhao, Y. Wang and Y. Liu, *Adv. Funct. Mater.*, 2023, **33**, 2304316.

45 N. Zhang, W. Li, J. Zhu, T. Wang, R. Zhang, K. Chi, Y. Liu, Y. Zhao and X. Lu, *Adv. Mater.*, 2023, **35**, 2300094.

46 T. Duan, Y. Wu, K. Yang, J. Oh, C. Yang, S. Chen, C. Zhong, D. Yu, Y. Zhao and S. Lu, *J. Mater. Chem. C*, 2021, **9**, 13625–13629.

47 Z. Li, X. Li, J. Xue, J. Zhang, C. Zhu, J. Li, W. Ma, L. Meng and Y. Li, *ACS Energy Lett.*, 2023, **8**, 2488–2495.

48 C. Li, J. Zhou, J. Song, J. Xu, H. Zhang, X. Zhang, J. Guo, L. Zhu, D. Wei, G. Han, J. Min, Y. Zhang, Z. Xie, Y. Yi, H. Yan, F. Gao, F. Liu and Y. Sun, *Nat. Energy*, 2021, **6**, 605–613.

49 Y. Wang, D. Qian, Y. Cui, H. Zhang, J. Hou, K. Vandewal, T. Kirchartz and F. Gao, *Adv. Energy Mater.*, 2018, **8**, 1801352.

50 W. Feng, T. Chen, Y. Li, T. Duan, X. Jiang, C. Zhong, Y. Zhang, J. Yu, G. Lu, X. Wan, B. Kan and Y. Chen, *Angew. Chem., Int. Ed.*, 2024, **63**, e202316698.

51 C. Zhang, J. Li, W. Deng, J. Dai, J. Yu, G. Lu, H. Hu and K. Wang, *Adv. Funct. Mater.*, 2023, **33**, 2301108.

52 K. Liu, Y. Jiang, G. Ran, F. Liu, W. Zhang and X. Zhu, *Joule*, 2024, **8**, 835–851.

53 X. Liu, Z. Zhang, C. Wang, C. Zhang, S. Liang, H. Fang, B. Wang, Z. Tang, C. Xiao and W. Li, *Angew. Chem., Int. Ed.*, 2024, **63**, e202316039.